symmetry

MDPI

Article

Structural Properties of Vicsek-like Deterministic Multifractals

Eugen Mircea Anitas [1,2,*], Giorgia Marcelli [3], Zsolt Szakacs [4], Radu Todoran [4] and Daniela Todoran [4]

1 Bogoliubov Laboratory of Theoretical Physics, Joint Institute for Nuclear Research, 141980 Dubna, Russian
2 Horia Hulubei, National Institute of Physics and Nuclear Engineering, 77125 Magurele, Romania
3 Faculty of Mathematical, Physical and Natural Sciences, Sapienza University of Rome, 00185 Rome, Italy; marcelli.giorgia@gmail.com
4 Faculty of Science, Technical University of Cluj Napoca, North University Center of Baia Mare, Baia Mare, 430122 Maramures, Romania; szakacsz@yahoo.com (Z.S.); todoran_radu@yahoo.com (R.T.); todorandaniela05@yahoo.com (D.T.)
* Correspondence: anitas@theor.jinr.ru

Received: 13 May 2019; Accepted: 15 June 2019; Published: 18 June 2019

Abstract: Deterministic nano-fractal structures have recently emerged, displaying huge potential for the fabrication of complex materials with predefined physical properties and functionalities. Exploiting the structural properties of fractals, such as symmetry and self-similarity, could greatly extend the applicability of such materials. Analyses of small-angle scattering (SAS) curves from deterministic fractal models with a single scaling factor have allowed the obtaining of valuable fractal properties but they are insufficient to describe non-uniform structures with rich scaling properties such as fractals with multiple scaling factors. To extract additional information about this class of fractal structures we performed an analysis of multifractal spectra and SAS intensity of a representative fractal model with two scaling factors—termed Vicsek-like fractal. We observed that the box-counting fractal dimension in multifractal spectra coincide with the scattering exponent of SAS curves in mass-fractal regions. Our analyses further revealed transitions from heterogeneous to homogeneous structures accompanied by changes from short to long-range mass-fractal regions. These transitions are explained in terms of the relative values of the scaling factors.

Keywords: fractals; small-angle scattering; form factor; structural properties; dimension spectra; pair distance distribution function

1. Introduction

Recent progress in materials science and nanotechnology has opened new possibilities in the production of new types of nano- and micro-structured materials with improved functions and properties [1–7], thus providing links to both deterministic classical mechanics and chaotic quantum mechanics [8,9]. Since the physical characteristics greatly depend on their structure, one of the main challenges in the field of materials science is to understand the correlation between them on a broad spectrum of length scales, starting from atomic level. In particular, for many nanoscale structures, quantum-like properties are frequently observable, thus displaying many interesting nano-effects [10–12]. However, for some materials, such as electrospun nanofibers, it has been shown that these effects depend strongly upon their fractal structure [9].

Therefore, ongoing research is carried out to obtain structures with exact self-similar (ESS) properties [13–19], where an intrinsic pattern repeats itself *exactly* under scaling. This procedure usually leads to highly symmetric fractal structures, such as Cantor dust, Sierpinski carpet or Menger

sponge [20]. In the field of chaotic deterministic systems they are known as strange attractors, since they may represent a set of infinite unconnected points (Cantor dust), a pathological curve (Weierstrass function) which is continuous everywhere but differentiable nowhere, or generally any geometric shape that cannot be easily described with a simple set operations of basic geometric objects.

ESS nano- and micro-materials attract a lot of attention due to their improved physical characteristics as compared with classical ones, and which arise mainly due to their symmetry and self-similar properties [21]. For example, the mechanical performance of 3D printed biomimetic Koch fractals interlocking can be effectively increased via fractal design [22], while the radiative heat flux can be kept at a short range (as compared to non-fractal structures) in ESS-based materials [23]. However, one of the main challenges in building such fractal materials is finding the suitable mixing composition between the embedding matrix and the fractal's material. To date, only a few materials have been successfully used to create such ESS structures, including dicarbonitrile [24] and bys-terpyridine molecules [13], single/poly crystalline silicone [14,15] or alkyletene dimers [25].

The structural properties of this new generation of nano- and micro-scale materials can effectively be determined using the small-angle scattering (SAS) of X-rays (SAXS) or neutrons (SANS) [26,27]. This widely used material-morphology investigation method has the advantage of sampling a statistically significant macroscopic volume. For ESS structures, the main advantage of SAS relies on its ability to distinguish between mass and surface fractals through the value of the scattering exponent τ in the fractal region [28–31]. More recently, it has been shown that SAS can also differentiate between ESS and statistically self-similar (SSS) structures [32] as well as between regular and fat fractals, that is, those with positive Lebesgue measure [33].

However, the behavior of the SAS intensity curves obtained from multifractals, that is, structures obtained by intermixing fractals with several scaling factors, are not yet completely understood. This is mainly due to the fact that the vast majority of physical materials are heterogeneous at nano- and micro-scales, thus requiring models with at least two scaling factors. Although a first step in this direction was done by obtaining the SAS spectrum from a multifractal structure generated using the chaos game algorithm [34], an expression for the scattering intensity was derived only recently [32]. Moreover, in Reference [34] it has been shown that, for the investigated structure, the oscillations in the fractal region are not very pronounced leading to difficulties in recovering the scaling factors from experimental data. This is an intrinsic consequence of the model's construction procedure, which involves a random variable in generating the positions of the fractal scattering units, as well as the presence of multiple scaling factors.

The purpose of this work is to provide a description of how to extract the scaling factor(s) from SAS data and how to relate them to the degree of fractal's heterogeneity. To this aim, in Section 2.1 we briefly describe the multifractals together with the moment method used to calculate the dimension spectra. Section 2.2 presents the main concepts of SAS with a focus on the form factor, pair distance distribution function (pddf) and their properties. In Section 3.1 we describe the construction process of the Vicsek-like multifractal model with two variable scaling factors [35,36] and show how one can obtain analytically the box-counting fractal dimension. In Section 3.2 we calculate numerically the corresponding dimension spectra and compare them with the theoretical results. In Section 3.3 we obtain the coefficients of the pddf. Finally, Section 3.4 presents an analytical expression of the form factor together with the influence of the polydispersity. Here, we also relate the behavior of the form factor with information from dimension spectra from Section 3.2.

2. Theoretical Background

2.1. Multifractals

Multifractals are non-uniform structures with rich scaling and self-similar properties that can change at every point [37,38]. A common procedure used to investigate their properties is to calculate their dimension spectrum. For this purpose several methods can be used, such as moment method [39], multifractal detrended fluctuation analysis [40] or wavelet transform modulus

maxima [41]. Here, we make use of the moment method due to its simplicity of implementation in a computer code as well as for its general applicability. An advantage of this method is that it is particularly well suited for analysis of images acquired by various methods including atomic force microscopy, scanning electron microscopy, computed tomography etc.

For this purpose, let us consider first an object S covered by a grid of boxes $B_i(l)$ of size l and a measure $\mu(B)$ determined by the probability of hitting the object in the box B_i. The corresponding partition function Z_s is defined by [41]:

$$Z_s(l) = \sum_{i=1}^{N} p_i^s(l), \tag{1}$$

where $N \propto 1/l^2$ is the number of boxes, i indexes each individual box, and $p_i = \mu(B)$ represent probabilities with r_i fragmentation ratios, such that $\sum_{i=1}^{N} p_i = 1$.

In terms of the partition function, the generalized dimension spectrum D_s can be written as [41]:

$$D_s \equiv \frac{1}{1-s} \lim_{l \to 0} \frac{\ln Z_s(l)}{-\ln l}, \tag{2}$$

where we take into account that Z_s has a power-law behavior in the limit $l \to 0$ and $N \to \infty$, so that $Z_s \propto l^{D_s(s-1)}$. Therefore:

$$D_s = \lim_{l \to 0} \frac{1}{1-s} \frac{\ln \sum_{i=1}^{N} p_i^s(l)}{-\ln l}, \tag{3}$$

with $p_i \equiv N_i(l)/N$ being the relative weight of the i-th box. In practice, dimension spectra can be obtained from images acquired using various techniques, such as atomic force microscopy, scanning electron microscopy, computed tomography and so on. Thus the quantity N_i in defining the probabilities p_i, is given by the number of non-white pixels in the i-th box, while N is the total number of pixels in the image.

The function D_s is a monotonically decreasing one, with the horizontal asymptotes $\alpha_{max} = \lim_{s \to -\infty} D_s$ and $\alpha_{min} = \lim_{s \to \infty} D_s$. The quantities α_{max} and α_{min} describe the scaling properties of the most rarefied, and respectively of the most dense regions in the fractal. Thus, the object is homogeneous if $\alpha_{max} = \alpha_{min}$, so that it becomes a single scale fractal, and the corresponding D_s spectrum is a line. In particular, at $s = 0$ one recover the well-known box-counting dimension, since it gives:

$$D_0 = \lim_{l \to 0} \frac{\log N(l)}{-\log l}, \tag{4}$$

with $s \equiv D_0$ and $l = \delta$. Here, $N(l)$ is the number of boxes in the minimal cover. At $s = 1$, D_1 gives a description of how the morphology increases as $l \to 0$, and thus is called the information dimension. After applying L'Hopital's rule, D_1 can be written as:

$$D_1 = \lim_{l \to 0} \frac{\sum_{i=1}^{N} p_i \log p_i}{-\log l}, \tag{5}$$

which is related to Shannon's entropy and measures how the information scales with $1/l$. The higher the values of fractal dimension D_1, the more uniform the density. At $s = 2$, Equation (3) gives D_2, which is called the *two-point correlation dimension* and is a measure of the correlation between pairs of points in each box. It describes how the data are scattered, with higher values of D_2 corresponding to higher compactness.

2.2. Small-Angle Scattering

SAS technique is based on the interaction of an incident beam with the electrons in the sample (for SAXS), respectively with the atomic nuclei (for SANS). Since neutrons interact with the magnetic moments, they also provide important information about the sample material's magnetic

properties. Therefore, SAS describes spatial density-density correlations in materials through a Fourier transform, leading to the determination of the differential elastic cross section $\mathrm{d}\sigma/\mathrm{d}\Omega$. When this quantity is normalized with regard to the irradiated volume $V^{'}$, it gives the scattering intensity [26] $I(q) = (1/V^{'})\mathrm{d}\sigma/\mathrm{d}\Omega$ as a function of the momentum transfer $q = 4\pi\lambda^{-1}\sin\theta$, where λ is the incident beam's wavelength and 2θ the scattering angle. Although in this low-resolution technique the phase information is lost, a more detailed structural description can be obtained when it is complemented by data obtained from other methods, such as protein crystallography [42], nuclear magnetic resonance [43], or when numerical procedures are used to recover the phase, as in coherent SAXS [44]. Let us consider a volume $V^{'}$ irradiated by a beam of light, X-ray, or neutrons, which contains the matrix, with a scattering length density (SLD) ρ_{p}, together with a large number of randomly oriented, non-interacting multifractals, with uncorrelated positions. Denoting by ρ_{m} the SLD of the fractals, after subtracting the matrix density, we can consider a system of scattering units "frozen" in vacuum. It has a scattering density of $\Delta\rho = \rho_{\mathrm{m}} - \rho_{\mathrm{p}}$, called the scattering contrast. Thus, denoting by n the concentration of the fractals, the scattering intensity is given by [26]:

$$I(q) = n|\Delta\rho|^2 V^2 \left\langle |F(\boldsymbol{q})|^2 \right\rangle, \tag{6}$$

where V is each fractal's volume, $F(\boldsymbol{q})$ is the form factor:

$$F(\boldsymbol{q}) \equiv \frac{1}{V}\int_V e^{-i\boldsymbol{q}\cdot\boldsymbol{r}}\mathrm{d}\boldsymbol{r}, \tag{7}$$

obeying the boundary condition $F(0) = 1$. The symbol $\langle\cdots\rangle$ stands for ensemble averaging over all orientations of the fractal, which, for an arbitrary two-dimensional function f, is defined as:

$$\left\langle f(q_x, q_y)\right\rangle = \frac{1}{2\pi}\int_0^{2\pi} f(q,\phi)\mathrm{d}\phi. \tag{8}$$

For a mass fractal with fractal dimension D_{m}, total length L, composed of p basic units, each of size l, separated by the distance d, so that $l \lesssim d \lesssim L$, the normalized form factor in Equation (7) can be written as:

$$\left\langle |F^{(\mathrm{m})}(\boldsymbol{q})|^2 \right\rangle \simeq \begin{cases} 1, & q \lesssim 2\pi/L, \\ (qL/2\pi)^{-D_{\mathrm{m}}}, & 2\pi/L \lesssim q \lesssim 2\pi/h, \\ 1/p, & 2\pi/h \lesssim q \lesssim 2\pi/l, \\ (1/p)\,(qL/2\pi)^{-4}, & 2\pi/l \lesssim q, \end{cases} \tag{9}$$

where p is of the order of $(L/h)^{D_{\mathrm{m}}}$. The four intervals in the definition of this piecewise function delimit the main structural regions on a double logarithmic scale: the plateau at low q is the Guinier region, the simple power-law decay is the fractal region, a second plateau, and finally the Porod region represented by a power-law decay with scattering exponent -4, or respectively -3 for 2D structures. Because we are dealing with a model for which the distances between the objects is of the same order of magnitude as their size, so that $d/l \simeq 1$, the second plateau from Equation (9) will not be observed. This shall be of no concern to us, since we are extracting structural information from the fractal region.

In calculating the SAS curves one makes use of the following properties of the form factor defined in Equation (7):

- $F(\boldsymbol{q}) \to F(\beta\boldsymbol{q})$ if the particle's length is scaled as $L \to \beta L$,
- $F(\boldsymbol{q}) \to F(\boldsymbol{q})e^{-i\boldsymbol{q}\cdot\boldsymbol{a}}$ if the particle is translated by the vector $\boldsymbol{r} \to \boldsymbol{r} + \boldsymbol{a}$,
- $F(\boldsymbol{q}) = \left[V_I F_I(\boldsymbol{q}) + V_{II}F_{II}(\boldsymbol{q})\right] / \left(V_I + V_{II}\right)$, if the particle can be decomposed as a union of two non-overlapping subsets I and II.

It is known that for a single-scale mass fractal consisting of k units (here disks will be used) at the m-th iteration, each with a form factor F_0, the scattering intensity can be written as [30]:

$$I(q) = I(0)S(q)\left\langle |F_0(\boldsymbol{q})|^2 \right\rangle / k^m, \tag{10}$$

where $S(q)$ is the structure factor, defined by:

$$S(q) \equiv \left\langle \rho_{\boldsymbol{q}} \rho_{-\boldsymbol{q}} \right\rangle / k^m, \tag{11}$$

and is related to the pddf $p(r)$ through:

$$S(q) = 1 + (k^m - 1)\int_0^{+\infty} \mathrm{d}r p(r) \frac{\sin qr}{qr}. \tag{12}$$

For single scale mass-fractals, the function $p(r)$ appearing in Equation (12) is the probability density of finding the distance r between the centers of two arbitrarily taken disks inside the fractal, and is defined by the following expression [30]:

$$p(r) = \frac{2}{k^m\,(k^m - 1)} \sum_{r_p} C_p \delta(r - r_p), \tag{13}$$

where the symbol δ is the Dirac's delta function, $r_{jk} \equiv |\boldsymbol{r}_j - \boldsymbol{r}_k|$ is the relative distance between the centers of disk j and k, and C_p are the number of distances separated by r_p.

In a physical system, the scatterers have almost always a certain degree of polydispersity. Thus, in order to take into account this effect we consider that their size obey a distribution function $D_{\mathrm{N}}(l)$, defined in such a way that $D_{\mathrm{N}}(l)\mathrm{d}l$ gives the probability of the size of the fractal to be found in the interval $(l, l + \mathrm{d}l)$. In particular, we consider a log-normal distribution of the type:

$$D_{\mathrm{N}}(l) = \frac{1}{\sigma l (2\pi)^{1/2}} e^{-\frac{\left(\log(l/\mu) + \sigma^2/2\right)^2}{2\sigma^2}}, \tag{14}$$

with relative variance $\sigma_{\mathrm{r}} = (\langle l^2 \rangle_D - \mu^2)^{1/2}/\mu$, mean value $\mu = \langle l \rangle_D$, and variance $\sigma = \left(\log(1 + \sigma_{\mathrm{r}}^2)\right)^{1/2}$. Therefore, by using Equations (6) and (14) one obtains the polydisperse form factor averaged over the distribution function [26]:

$$I(q)/I(0) = \int_0^{\infty} \langle |F(\boldsymbol{q})|^2 \rangle A_m^2(l) D_{\mathrm{N}}(l) \mathrm{d}l, \tag{15}$$

where A_m is the corresponding area at mth iteration.

Thus, the scattering intensity given by Equation (15) leads to a simple power-law decay $I(q) \propto q^{-\tau}$, where $\tau = D_{\mathrm{m}}$ for mass fractals, and $\tau = 2d - D_{\mathrm{s}}$ for surface fractals. Recall that for mass fractals embedded in a d-dimensional Euclidean space we have $D_{\mathrm{s}} = D_{\mathrm{m}} < d$ and $D_{\mathrm{p}} = d$, while for surface fractals $D_{\mathrm{m}} = D_{\mathrm{p}} = d$ and $d - 1 < D_{\mathrm{s}} < d$. Here, D_{s} is the fractal dimension of the set's boundary, D_{m} is the set's "mass" fractal dimension, and D_{p} is the "pore" dimension of the surrounding matrix phase. Therefore, an object is classified as a mass fractal with $D_{\mathrm{m}} = \tau$ when the experimentally determined value of τ is smaller than d, while for $d - 1 < \tau < d$, it is a surface fractal with dimension $D_{\mathrm{s}} = 2d - \tau$ [45,46].

3. Results and Discussions

3.1. Construction of the Multifractal Model

In constructing the Vicsek-like [35] multifractal model one starts with a square of edge size l_0 in which we inscribe a disk of radius r_0, with $0 < r_0 < l_0/2$ such as that their centers coincide (Figure 1). This is called the zero-order iteration (i.e., $m = 0$), or the initiator. We choose a Cartesian system of

coordinates with the origin coinciding with the center of the square and disk, and axes parallel with the edges of the square. By replacing the initial disk with $k_1 = 4$ smaller disks of radii $r_1 = \beta_{s1} r_0$ situated in the corners of the square, and with $k_2 = 1$ disk of radius $r_2 = \beta_{s2} r_0$ situated in the center, we obtain the first iteration or generator ($m = 1$). Here, β_{s1} and β_{s2} are the scaling factors. The positions of the four corner disks are chosen in such a way that their centers are given by:

$$\boldsymbol{a}_j = \frac{1 - \beta_{s1}}{2} \{\pm l_0, \pm l_0\}, \tag{16}$$

with all combinations of the signs and with $j = 1, \cdots, 4$. The second fractal iteration ($m = 2$) is obtained by performing a similar operation on each of the $k_1 + k_2$ disks. For arbitrarily iterations m, the total number of disks is:

$$N_m = (k_1 + k_2)^m, \tag{17}$$

In the high m iteration number limit one obtains the multifractal, whose fractal dimension is given by [35]:

$$\sum_{i=1}^{2} k_i \beta_{si}^D = 1. \tag{18}$$

Note that the fractal dimension for the well-known Vicsek fractal is recovered for $\beta_{s1} = \beta_{s2} = 1/3$.

Figure 1 shows the first three iterations of the multifractal at various values of the scaling factors β_{s1} and β_{s2}. The different colors in Figure 1 represent the disks which arise at a given iteration number m. Black color denotes the disks arising at $m = 1$, orange those at $m = 2$, while green is used for the third iteration. The upper row from Figure 1 shows that for $\beta_{s1} = 0.1$ and $\beta_{s2} = 0.8$, denoted here model M1, a more heterogeneous structure is obtained when compared with the model M2 from the middle-row (i.e., for $\beta_{s1} = 0.2$ and $\beta_{s2} = 0.6$) or with the model M3 in the lower-raw, constructed using $\beta_{s1} = 0.3$ and $\beta_{s2} = 0.4$. It can also be noted that for model M3 the structure consists of very closely sized disks, and it resembles the single scale Vicsek fractal, as pointed out before.

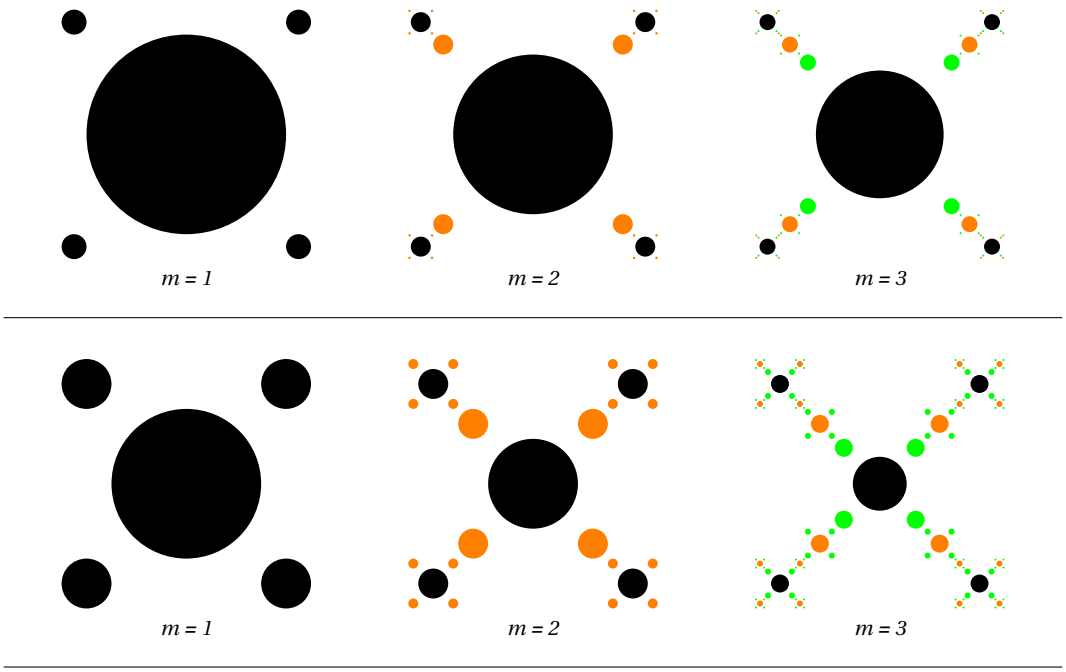

Figure 1. *Cont.*

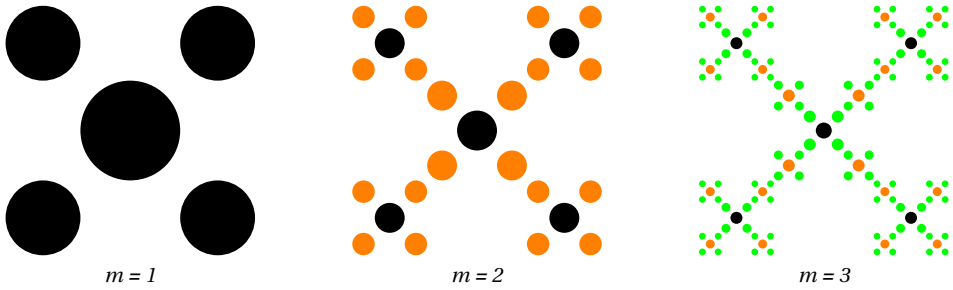

Figure 1. (Color online) First three iterations of the two-scale multifractal models. Upper row: $\beta_{s_1} = 0.1$ and $\beta_{s_2} = 0.8$ (Model M1). Note that for $m = 3$ the disks of radii $l_0\beta_{s_1}^3/2 = 0.0005l_0$ are too small to be seen in the figure (at the given size). Middle row: $\beta_{s_1} = 0.2$ and $\beta_{s_2} = 0.6$ (Model M2). Lower row: $\beta_{s_1} = 0.3$ and $\beta_{s_2} = 0.4$ (Model M3). Black, orange and green colors denote the disks generated at iterations $m = 1$, $m = 2$, and respectively at $m = 3$.

3.2. Dimension Spectra

The corresponding dimension spectra D_s for the three models M1, M2 and M3 are plotted using Equation (2) and can be seen in Figure 2 for $-10 < s < 10$. The spectrum for model M1 (black curve) clearly shows that D_s covers a broad range of values, with $0.15 \lesssim D_s \lesssim 1.85$. This can be explained by a high degree of heterogeneity, with the densest regions having the fractal dimension $\simeq 1.85$, while the most rarefied ones have dimension $\simeq 0.2$. The spectrum for model M2 (red curve) covers the much tighter range between $0.81 \lesssim D_s \lesssim 1.55$. But still, pronounced differences between regions with high and low densities are easily observed. The spectrum of model M3 (green curve) is almost a horizontal line, as expected, since the two scaling factors have close values, thus leading to an almost homogeneous fractal structure, with a fractal dimension of $D_s \simeq 1.42$. The vertical blue dotted line indicates the $s = 0$ axis. The box-counting dimensions of the three models can be determined using the intersection of the fractal dimension spectrum with this axis, so that: $D_0 \simeq 1.22$ (for model M1), $D_0 \simeq 1.31$ (for model M2) and $D_0 \simeq 1.42$ (for model M3).

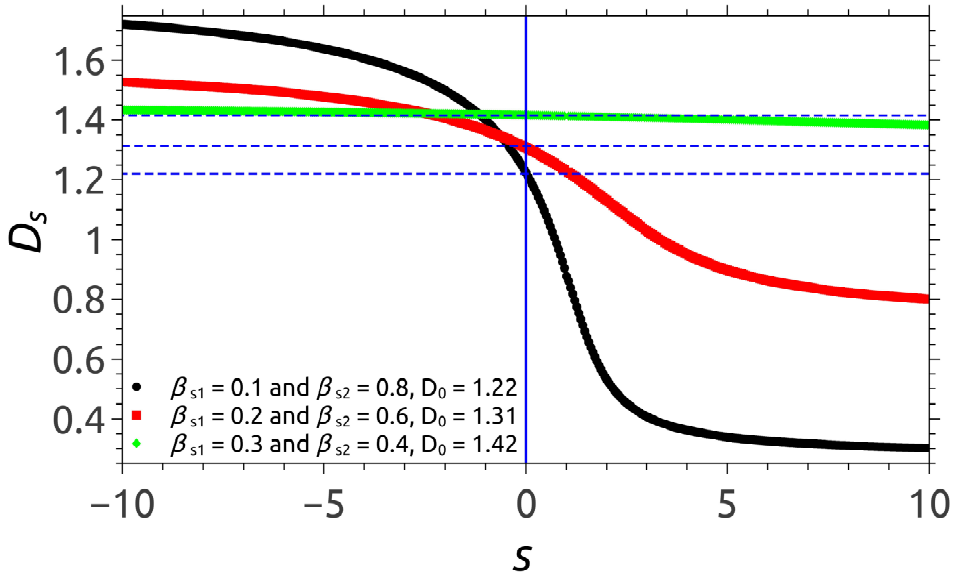

Figure 2. (Color online) Dimension spectra D_s for the three multifractal models: M1 (black), M2 (red), M3 (green). The intersection of the vertical line with each horizontal (dashed) line gives the box-counting dimension D_0.

3.3. Pair Distance Distribution Function

Figure 3 shows the real space characteristics for the same models M1, M2 and M3, at fractal iteration number $m = 4$ using the pddf function defined in Equation (13). The coefficients C_p are calculated numerically using simple combinatorial analysis. The general feature is the presence of distance-groups on a double logarithmic scale.

For $\beta_{s1} = 0.1$ and $\beta_{s2} = 0.8$ the periodicity is clearly visible (Figure 3a), the main groups being separated by gaps at $r/l_0 \simeq 4.5 \times 10^{-3}, 4.5 \times 10^{-2}$ and respectively at 4.5×10^{-1}, indicating the absence of the corresponding distances inside the fractal. The position of these groups is well described as having the periodicity $\log_{10}(1/\beta_{s1})$, and thus, they are related to the scaling factor β_{s1}. Inside each main group, other less pronounced smaller gaps can be noticed, which can be described as having a periodicity related to β_{s1}.

For models M2 and M3, when the scaling factors are relatively closer to each other, the gaps between main groups are less pronounced but still some periodicity can be seen (Figure 3b,c). However, the gaps within a single group are significantly smeared out (especially for model M3) and thus determining the scaling factor β_{s2} in these cases cannot be done with sufficient accuracy. This can be explained by the fact that when the scaling factors have close values, the position of the gaps corresponding to a scaling factor start to "interfere" with the positions of those corresponding to the other one. This leads to a more homogeneous structure, also reflected by the almost constant line in the dimension spectra of model M3 (the green curve from Figure 2).

3.4. Small-Angle Scattering Form Factor

In the proposed model, the positions of the four disks with scaling factor β_{s1} can be described by: $G_1(\boldsymbol{q}) = \cos(q_x l_0 (1 - \beta_{s1}/2)) \cos(q_y l_0 (1 - \beta_{s1}/2))$ while the position of the disk with scaling factor β_{s2} is given by $G_2(\boldsymbol{q}) = 1$. The total number of particles at m-th iteration is given by Equation (17), with $k_1 = 4$ and $k_2 = 1$, while the total surface area is $\left(k_1\beta_{s1}^2 + k_2\beta_{s2}\right)^m$. Thus, at $m = 1$, the fractal consists of k_1 disks of radius $r_1 = \beta_{s1} r_0$ and one disk of radius $r_2 = \beta_{s2} r_0$, with $r_0 = l_0/2$. Therefore, the form factor is given by:

$$F_1(\boldsymbol{q}) = \frac{k_1\beta_{s1}^2 G_1(\boldsymbol{q}) F_0(\beta_{s1}\boldsymbol{q}) + k_2\beta_{s2} G_2(\boldsymbol{q}) F_0(\beta_{s2}^2\boldsymbol{q})}{k_1\beta_{s1}^2 + k_2\beta_{s2}^2}, \tag{19}$$

where $F_0(q) = 2J_1(q)/q$ is the form factor of the disk, and $J_1(q)$ is the Bessel function of the first kind.

At $m = 2$, while repeating the same procedure for each disk, one obtains k_2 disks of radius $\beta_{s2}^2 r_0$, k_1 disks of radii $\beta_{s1}\beta_{s2} r_0$, k_1^2 disks of radii $\beta_{s2}^1 r_0$, k_1 and so on. Thus, at an arbitrarily iteration m, we can write the corresponding form factor in terms of a recurrence relation of the form [32]:

$$F_m(\boldsymbol{q}) = \frac{k_1\beta_{s1}^2 G_1(\boldsymbol{q}) F_{m-1}(\beta_{s1}\boldsymbol{q}) + k_2\beta_{s2} G_2(\boldsymbol{q}) F_{m-1}(\beta_{s2}^2\boldsymbol{q})}{k_1\beta_{s1}^2 + k_2\beta_{s2}^2}. \tag{20}$$

Thus, at arbitrary m, the scattering intensity (Equation (10)) can be written as:

$$I_m(q)/I_m(0) = \left\langle |F_m(\boldsymbol{q})|^2 \right\rangle, \tag{21}$$

Figure 4 shows the corresponding monodisperse (black curves) and polydisperse (red curves) scattering intensity for the multifractal models M1, M2 and M3. For calculating the polydispersity we used the log-normal distribution function given by Equation (14) with the relative variance $\sigma_r = 0.2$. One observes the presence of three main regions in each case. At $ql_0 \simeq \pi$ we have a Guinier region with $I(q) \propto q^0$. At $\pi \lesssim ql_0 \lesssim 2\pi/\beta_{s2}^m$ we have a mass fractal region with $I(q) \propto q^{-D_0}$, where D_0 is the box counting dimension of the multifractal, whose value coincides with that obtained from the dimension spectra (see Figure 2) and from Equation (18). At $2\pi/\beta_{s2}^m \gtrsim ql_0$ we are beyond the mass-fractal region, reaching the Porod regime with $I(q) \propto q^{-3}$. Here, the main region of interest is the

mass fractal one, since the exponent of the scattering intensity can be related to the multifractal spectra given in Figure 2.

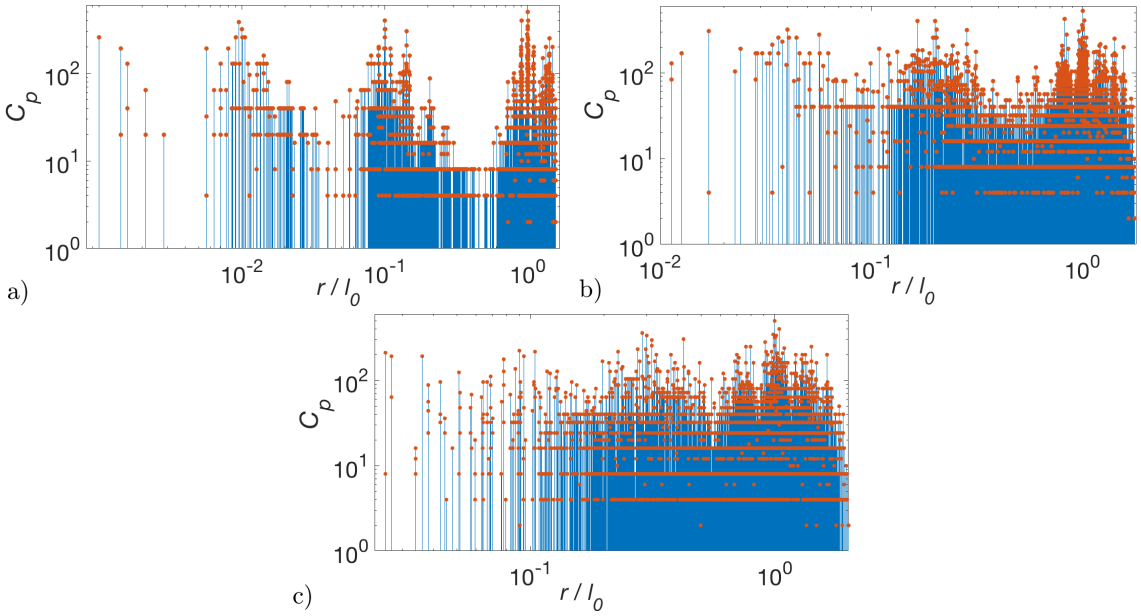

Figure 3. (Color online) The coefficients C_p (orange dots) in Equation (13) for the pair distribution function of the considered multifractal models at $m = 4$. (**a**) Model M1; (**b**) Model M2; (**c**) Model M3. For a better visualization of pddf grouping the vertical line (blue) for each distance is shown.

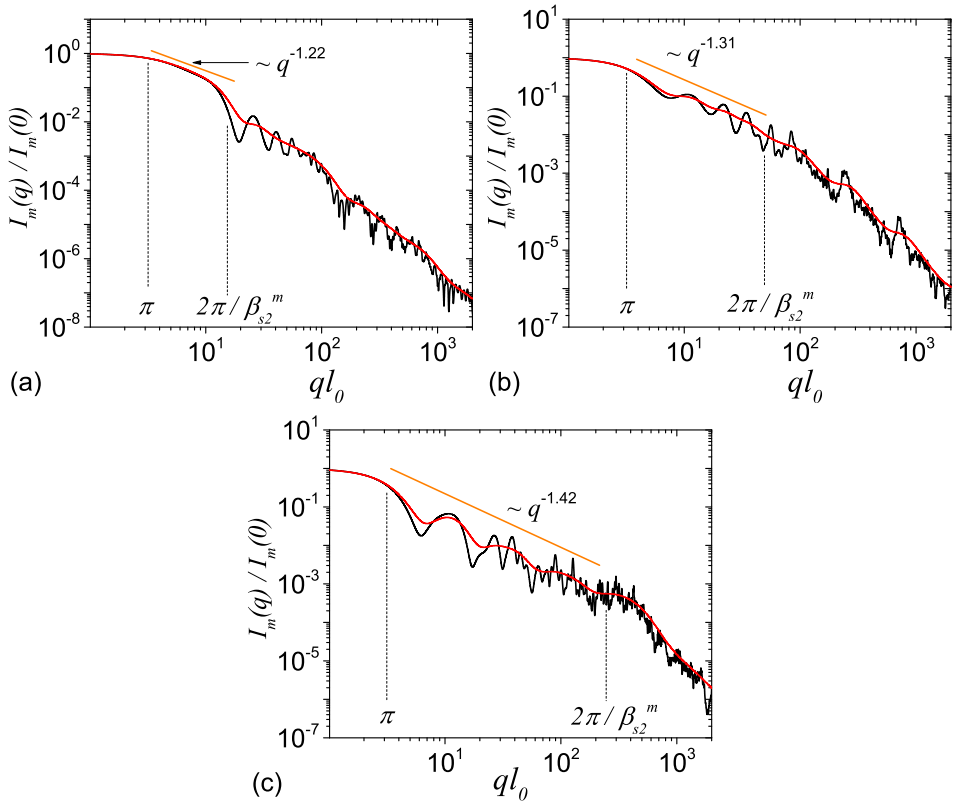

Figure 4. (Color online) Scattering form factor (Equation (21)) for monodisperse (black) and polydisperse (red) multifractal models at $m = 4$. (**a**) Model M1; (**b**) Model M2; (**c**) Model M3. Vertical lines indicate the lower and upper edges of mass fractal region.

These results show that, for the suggested model, the length of mass-fractal regions depends on the scaling factor β_{s2}, since $\beta_{s2} > \beta_{s1}$. The scattering from the three models M1, M2 and M3 illustrate three important cases. First, for the case of model M1, since $\beta_{s2} = 0.8$ is much larger than $\beta_{s1} = 0.1$, and they are related through $\beta_{s1} \equiv (1 - \beta_{s2})/2$, the upper edge of the mass fractal region is very close to its lower edge, so that no oscillations can be observed in this region (Figure 4a). However, when β_{s2} is of comparable size with β_{s1}, the length of the mass fractal region is enough large, so that a log-periodicity with the period $\log(1/\beta_{s1})$ can be observed (Figure 4a,b). In order to provide a better view of the log-periodicity, we show in Figure 5 the quantity $I(q)q^{D_0}$ vs. q. This also clearly shows the increasing complexity of the scattering curves in the fractal region, which arise due to mixing of structures of various sizes, corresponding to repeated subdivisions of the fractal with scaling factors β_{s1} and β_{s2}. In addition, for models M1 and M2 one can see that the number of most pronounced minima in the fractal region coincide with the fractal iteration number.

Note that in all cases, the corresponding polydisperse form factor smears the monodisperse curve. The degree to which the polydisperse curve is smeared-out depends on the value of the relative variance σ_r in the size distribution (Equation (14)): the higher the value of σ_r the more smooth the scattering curve. Therefore, as Figures 4 and 5 show, the periodicity and the number of fractal iteration can be recovered when the values of the relative variance are not very high.

For models M2 and M3, the relationships between the log-periodicity and the scaling factors are not so obvious as for model M1, due to superposition of maxima and minima arising from the 'mixing' of various structures of comparable sizes and of distances between them. This behavior is similar to the one observed in pddf, where separation of distance-groups is clearly visible only for model M1. Note that for 3D structures, the number of distances of a given value, is much higher than for the 2D model developed here, and thus, more pronounced minima and maxima shall be observed the SAS intensity for both the M2 and M3 models, along with more pronounced gaps in pddf.

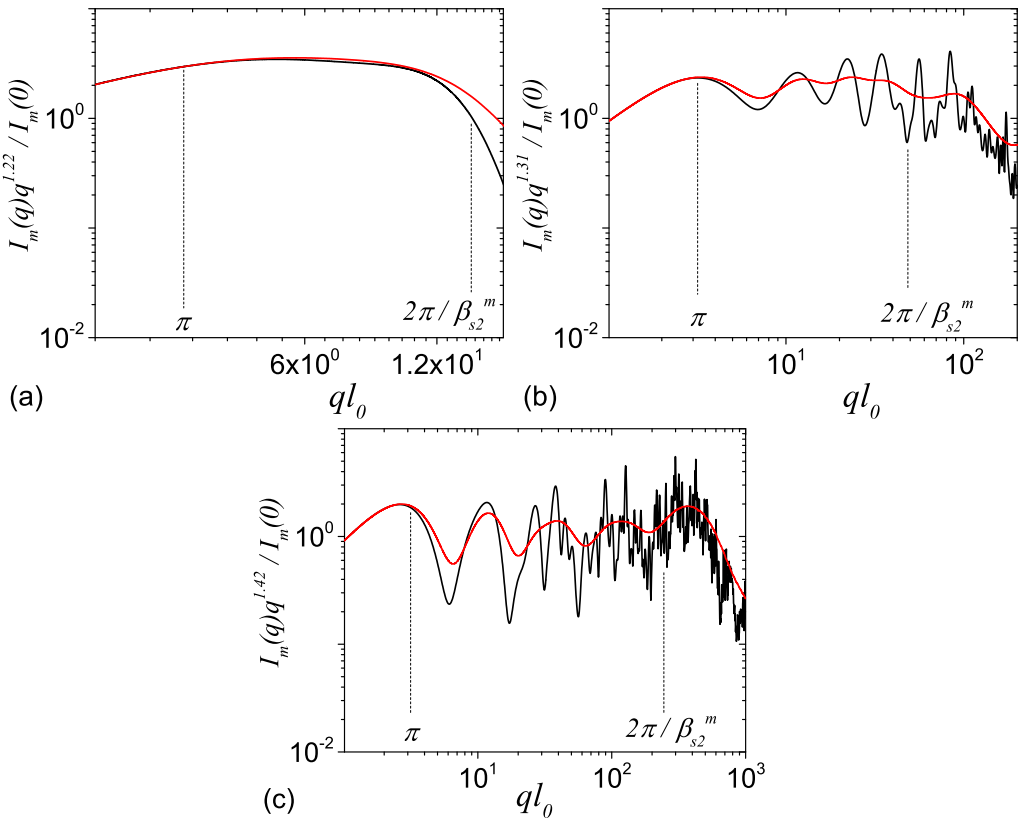

Figure 5. (Color online) The quantity $I(q)q^{D_0}$, where D_0 is the box-counting fractal dimension for monodisperse (black) and polydisperse (red) multifractal models at $m = 4$. (**a**) Model M1; (**b**) Model M2; (**c**) Model M3. Vertical lines indicate the lower and upper edges of the mass fractal region.

Therefore, a combined structural investigation involving SAXS/SANS experimental data, as well as an image analysis of multifractals, can be used to exploit the advantages provided by both reciprocal and real space. While for real space analysis the phase is not lost and thus the structure can be directly obtained, in the case of a reciprocal space analysis, the information is obtained from a macroscopic, statistically significant volume.

4. Conclusions

We developed a multifractal model that generalizes the well-known two-dimensional Vicsek fractal, with disks as basic units. The model is characterized by the presence of two-scaling factors β_{s1} and β_{s2} controlling the multifractal spectra and implicitly the box counting dimension D_0, in the range from 0 to 2.

Changes in the fractal heterogeneity are assessed using pddf and SAS intensity for several representative values of the scaling factors. The relative degree of heterogeneity is confirmed using the dimension spectra. However, depending on the relative values of the scaling factors, the changes can be more clearly visible in a particular space, that is, reciprocal or real. Thus, in order to extract additional structural information we identify three major situations, each one with its particular approach:

- If $\beta_{s1} << \beta_{s2}$, the system is highly heterogeneous and structural parameters are more clearly visible in pddf (see Figure 3a), since the mass fractal region of the scattering intensity is very short Figure 4a). The scaling factor β_{s1} is extracted from the periodicity of large groups of distances, while β_{s2} can be extracted in a relatively good approximation, from the periodicity of smaller groups found inside larger ones. The number of fractal iterations coincide with the number of large distinct groups in pddf.
- If $\beta_{s1} \lesssim \beta_{s2}$, separation of pddf in distinct groups of distance is not very clear since the values of distances arising from each of the scaling factors begin to mix with each other (see Figure 3b,c), and thus extracting exact values of the scaling factors can become a very difficult task. However, in the reciprocal space, the corresponding mass fractal region of scattering intensity is characterized by a succession of maxima and minima on a power-law decay (generalized power-law decay) and the value of the largest scaling factor can be clearly estimated from the periodicity of minima. In addition, the fractal dimension can be obtained from the scattering exponent of this power-law decay while the fractal iteration number can be obtained from the number of the minima.
- If $\beta_{s1} = \beta_{s2}$, the system reduces to a single scale fractal. Structural properties of such systems have been studied elsewhere (see Reference [30]).

Since multifractal spectra can be obtained by analyzing the images captured using various techniques, such as atomic force microscopy, scanning/transmission electron microscopy, computed tomography etc., a combined analysis of multifractal spectra together with SAS data can provide a route towards a more detailed structural analysis of multifractal structures at nano/micro-scales by exploiting the advantages provided by both real and reciprocal space analysis.

Author Contributions: Conceptualization, methodology, writing—original draft preparation, writing—review and editing, E.M.A.; investigation, formal analysis, validation, G.M.; supervision, Z.S., R.T. and D.T.

Funding: This research received no external funding. The APC was funded by Joint Institute for Nuclear Research.

Conflicts of Interest: The authors declare no conflict of interest.

References

1. Acosta, K.L.; Wilkie, W.K.; Inman, D.J. Characterizing the pyroelectric coefficient for macro-fiber composites. *Smart Mater. Struct.* **2018**, *27*, 115001. [CrossRef] [CrossRef]
2. Bica, I.; Anitas, E.M.; Lu, Q.; Choi, H.J. Effect of magnetic field intensity and γ-Fe2O3 nanoparticle additive on electrical conductivity and viscosity of magnetorheological carbonyl iron suspension-based membranes. *Smart Mater. Struct.* **2018**, *27*, 095021. [CrossRef] [CrossRef]

3. Theerthagiri, J.; Durai, G.; Karuppasamy, K.; Arunachalam, P.; Elakkiya, V.; Kuppusami, P.; Maiyalagan, T.; Kim, H.S. Recent advances in 2-D nanostructured metal nitrides, carbides, and phosphides electrodes for electrochemical supercapacitors—A brief review. *J. Ind. Eng. Chem.* **2018**, *67*, 12–27. [CrossRef] [CrossRef]
4. Kim, K.W.; Ji, S.H.; Park, B.S.; Yun, J.S. High surface area flexible zeolite fibers based on a core-shell structure by a polymer surface wet etching process. *Mater. Des.* **2018**, *158*, 98–105. [CrossRef] [CrossRef]
5. Semitekolos, D.; Kainourgios, P.; Jones, C.; Rana, A.; Koumoulos, E.P.; Charitidis, C.A. Advanced carbon fibre composites via poly methacrylic acid surface treatment; surface analysis and mechanical properties investigation. *Compos. Part B—Eng.* **2018**, *155*, 237–243. [CrossRef] [CrossRef]
6. Anagnostou, D.; Chatzigeorgiou, G.; Chemisky, Y.; Meraghni, F. Hierarchical micromechanical modeling of the viscoelastic behavior coupled to damage in SMC and SMC-hybrid composites. *Compos. Part B—Eng.* **2018**, *151*, 8–24. [CrossRef] [CrossRef]
7. Bica, I.; Anitas, E.M. Magnetic flux density effect on electrical properties and visco-elastic state of magnetoactive tissues. *Compos. Part B—Eng.* **2019**, *159*, 13–19. [CrossRef] [CrossRef]
8. El Naschie, M.S. Nanotechnology for the developing world. *Chaos Soliton Fract.* **2006**, *30*, 769. [CrossRef] [CrossRef]
9. He, J.H.; Wan, Y.Q.; Xu, L. Nano-effects, quantum-like properties in electrospun nanofibers. *Chaos Soliton Fract.* **2007**, *33*, 26–37. [CrossRef] [CrossRef]
10. Zhang, Z.; Gao, C.; Wu, Z.; Han, W.; Wang, Y.; Fu, W.; Li, X.; Xie, E. Toward efficient photoelectrochemical water-splitting by using screw-like SnO_2 nanostructures as photoanode after being decorated with CdS quantum dots. *Nano Energy* **2016**, *19*, 318–327. [CrossRef] [CrossRef]
11. Sichert, J.A.; Tong, Y.; Mutz, N.; Vollmer, M.; Fischer, S.; Milowska, K.Z.; García Cortadella, R.; Nickel, B.; Cardenas-Daw, C.; Stolarczyk, J.K.; et al. Quantum Size Effect in Organometal Halide Perovskite Nanoplatelets. *Nano Lett.* **2015**, *15*, 6521–6527. [CrossRef] [CrossRef] [PubMed]
12. Zhu, W.; Esteban, R.; Borisov, A.G.; Baumberg, J.J.; Nordlander, P.; Lezec, H.J.; Aizpurua, J.; Crozier, K.B. Quantum mechanical effects in plasmonic structures with subnanometre gaps. *Nat. Commun.* **2016**, *7*, 11495. [CrossRef] [CrossRef] [PubMed]
13. Newkome, G.R.; Wang, P.; Moorefield, C.N.; Cho, T.J.; Mohapatra, P.P.; Li, S.; Hwang, S.H.; Lukoyanova, O.; Echegoyen, L.; Palagallo, J.A.; et al. Nanoassembly of a fractal polymer: A molecular "Sierpinski hexagonal gasket". *Science* **2006**, *312*, 1782–1785. [CrossRef] [CrossRef] [PubMed]
14. Cerofolini, G.F.; Narducci, D.; Amato, P.; Romano, E. Fractal Nanotechnology. *Nanoscale Res. Lett.* **2008**, *3*, 381–385. [CrossRef] [CrossRef]
15. Berenschot, E.J.W.; Jansen, H.V.; Tas, N.R. Fabrication of 3D fractal structures using nanoscale anisotropic etching of single crystalline silicon. *J. Micromech. Microeng.* **2013**, *23*, 055024. [CrossRef] [CrossRef]
16. Li, C.; Zhang, X.; Li, N.; Wang, Y.; Yang, J.; Gu, G.; Zhang, Y.; Hou, S.; Peng, L.; Wu, K.; et al. Construction of Sierpiński Triangles up to the Fifth Order. *J. Am. Chem. Soc.* **2017**, *139*, 13749–13753. [CrossRef] [CrossRef] [PubMed]
17. Li, N.; Zhang, X.; Gu, G.C.; Wang, H.; Nieckarz, D.; Szabelski, P.; He, Y.; Wang, Y.; Lü, J.T.; Tang, H.; et al. Sierpiński-triangle fractal crystals with the C3v point group. *Chin. Chem. Lett.* **2015**, *26*, 1198–1202. [CrossRef] [CrossRef]
18. Zhang, X.; Li, R.; Li, N.; Gu, G.; Zhang, Y.; Hou, S.; Wang, Y. Sierpiński triangles formed by molecules with linear backbones on Au(111). *Chin. Chem. Lett.* **2018**, *29*, 967–969. [CrossRef] [CrossRef]
19. Fan, J.A.; Yeo, W.H.; Su, Y.; Hattori, Y.; Lee, W.; Jung, S.Y.; Zhang, Y.; Liu, Z.; Cheng, H.; Falgout, L.; et al. Fractal design concepts for stretchable electronics. *Nat. Commun.* **2014**, *5*, 3266. [CrossRef] [CrossRef]
20. Mandelbrot, B.B. *The Fractal Geometry of Nature*; W.H. Freeman: New York, NY, USA, 1982; p. 460.
21. Filoche, M.; Sapoval, B. Transfer Across Random versus Deterministic Fractal Interfaces. *Phys. Rev. Lett.* **2000**, *84*, 5776–5779. [CrossRef] [CrossRef]
22. Khoshhesab, M.M.; Li, Y. Mechanical behavior of 3D printed biomimetic Koch fractal contact and interlocking. *Extrem. Mech. Lett.* **2018**, *24*, 58–65. [CrossRef] [CrossRef]
23. Nikbakht, M. Radiative heat transfer in fractal structures. *Phys. Rev. B* **2017**, *96*, 125436. [CrossRef] [CrossRef]
24. Zhang, B.; Xiang, M.; Zhang, Q.; Zhang, Q. Preparation and characterization of bioinspired three-dimensional architecture of zirconia on ceramic surface. *Compos. Part B—Eng.* **2018**, *155*, 77–82. [CrossRef] [CrossRef]
25. Mayama, H.; Tsujii, K. Menger sponge-like fractal body created by a novel template method. *J. Chem. Phys.* **2006**, *125*, 124706. [CrossRef] [CrossRef] [PubMed]

26. Feigin, L.A.; Svergun, D.I. *Structure Analysis by Small-Angle X-ray and Neutron Scattering*; Springer: Boston, MA, USA, 1987; p. 335. [CrossRef]
27. Gille, W. *Particle and Particle Systems Characterization: Small-Angle Scattering (SAS) Applications*, 1st ed.; CRC Press: Boca Raton, FL, USA, 2013; p. 336.
28. Teixeira, J. Small-angle scattering by fractal systems. *J. Appl. Cryst.* **1988**, *21*, 781–785. [CrossRef] [CrossRef]
29. Schmidt, P.W.; Dacai, X. Calculation of the small-angle x-ray and neutron scattering from nonrandom (regular) fractals. *Phys. Rev. A* **1986**, *33*, 560–566. [CrossRef] [CrossRef]
30. Cherny, A.Y.; Anitas, E.M.; Osipov, V.A.; Kuklin, A.I. Deterministic fractals: Extracting additional information from small-angle scattering data. *Phys. Rev. E* **2011**, *84*, 036203. [CrossRef] [CrossRef] [PubMed]
31. Anitas, E.M.; Slyamov, A.M. Small-angle scattering from deterministic mass and surface fractal systems. *Proc. Rom. Acad. A* **2018**, *19*, 353–360.
32. Cherny, A.Y.; Anitas, E.M.; Osipov, V.A.; Kuklin, A.I. The structure of deterministic mass and surface fractals: Theory and methods of analyzing small-angle scattering data. *Phys. Chem. Chem. Phys.* **2019**. [CrossRef] [CrossRef]
33. Anitas, E.M.; Slyamov, A.; Todoran, R.; Szakacs, Z. Small-Angle Scattering from Nanoscale Fat Fractals. *Nanoscale Res. Lett.* **2017**, *12*, 389. [CrossRef] [CrossRef]
34. Anitas, E.M.; Slyamov, A. Structural characterization of chaos game fractals using small-angle scattering analysis. *PLoS ONE* **2017**, *12*, e0181385. [CrossRef] [CrossRef] [PubMed]
35. Vicsek, T. *Fractal Growth Phenomena*, 2nd ed.; World Scientific: Singapore, 1992; p. 528. [CrossRef]
36. Gouyet, J.F. *Physics and Fractal Structures*; Elsevier: Masson, UK, 1996; p. 234.
37. Arneodo, A.; Decoster, N.; Roux, S. A wavelet-based method for multifractal image analysis. I. Methodology and test applications on isotropic and anisotropic random rough surfaces. *Eur. Phys. J. B* **2000**, *15*, 567–600. [CrossRef] [CrossRef]
38. Decoster, N.; Roux, S.; Arnéodo, A. A wavelet-based method for multifractal image analysis. II. Applications to synthetic multifractal rough surfaces. *Eur. Phys. J. B* **2000**, *15*, 739–764. [CrossRef] [CrossRef]
39. Chhabra, A.; Jensen, R.V. Direct Determination of the f (alpha) Singularity Spectrum. *Phys. Rev. Lett.* **1989**, *62*, 1327. [CrossRef] [PubMed]
40. Kantelhardt, J.W.; Zschiegner, S.A.; Koscielny-Bunde, E.; Havlin, S.; Bunde, A.; Stanley, H. Multifractal detrended fluctuation analysis of nonstationary time series. *Phys. A* **2002**, *316*, 87–114. [CrossRef] [CrossRef]
41. Muzy, J.F.; Bacry, E.; Arneodo, A. Multifractal formalism for fractal signals: The structure-function approach versus the wavelet-transform modulus-maxima method. *Phys. Rev. E* **1993**, *47*, 875–884. [CrossRef] [CrossRef]
42. Stuhrmann, H.B. Small-angle scattering and its interplay with crystallography, contrast variation in SAXS and SANS. *Acta Cryst.* **2008**, *64*, 181–191. [CrossRef] [CrossRef]
43. Izumi, A.; Shudo, Y.; Nakao, T.; Shibayama, M. Cross-link inhomogeneity in phenolic resins at the initial stage of curing studied by 1H-pulse NMR spectroscopy and complementary SAXS/WAXS and SANS/WANS with a solvent-swelling technique. *Polymer* **2016**, *103*, 152–162. [CrossRef] [CrossRef]
44. Dierolf, M.; Menzel, A.; Thibault, P.; Schneider, P.; Kewish, C.M.; Wepf, R.; Bunk, O.; Pfeiffer, F. Ptychographic X-ray computed tomography at the nanoscale. *Nature* **2010**, *467*, 436–439. [CrossRef] [CrossRef]
45. Martin, J.E.; Hurd, A.J. Scattering from fractals. *J. Appl. Cryst.* **1987**, *20*, 61–78. [CrossRef] [CrossRef]
46. Schmidt, P.W. Small-angle scattering studies of disordered, porous and fractal systems. *J. Appl. Cryst.* **1991**, *24*, 414–435. [CrossRef] [CrossRef]